

Ultrasensitive Strain Gauges Enabled by Graphene-Stabilized Silicone Emulsions

Marcus A. O'Mara,* Sean P. Ogilvie, Matthew J. Large, Aline Amorim Graf, Anne C. Sehnal, Peter J. Lynch, Jonathan P. Salvage, Izabela Jurewicz, Alice A. K. King, and Alan B. Dalton*

Here, an approach is presented to incorporate graphene nanosheets into a silicone rubber matrix via solid stabilization of oil-in-water emulsions. These emulsions can be cured into discrete, graphene-coated silicone balls or continuous, elastomeric films by controlling the degree of coalescence. The electromechanical properties of the resulting composites as a function of interdiffusion time and graphene loading level are characterized. With conductivities approaching 1 S m^{-1} , elongation to break up to 160%, and a gauge factor of ≈ 20 in the low-strain linear regime, small strains such as pulse can be accurately measured. At higher strains, the electromechanical response exhibits a robust exponential dependence, allowing accurate readout for higher strain movements such as chest motion and joint bending. The exponential gauge factor is found to be ≈ 20 , independent of loading level and valid up to 80% strain; this consistent performance is due to the emulsion-templated microstructure of the composites. The robust behavior may facilitate high-strain sensing in the nonlinear regime using nanocomposites, where relative resistance change values in excess of 10^7 enable highly accurate bodily motion monitoring.

transparent, durable, and has very minimal shrinkage on curing. As a result, PDMS has become ubiquitous in health-care, aerospace, food, and microfluidics industries.^[1–3] One property of PDMS that presents a challenge when seeking to produce nanocomposites with desirable properties is the high rotational freedom of the polymer backbone. This allows methyl groups with characteristically low surface energy ($\approx 50 \text{ mN m}^{-1}$) and chemical reactivity to present themselves at interfaces. The consequence is that homogeneous dispersion of layered nanomaterials ($\approx 70 \text{ mN m}^{-1}$)^[4,5] within a PDMS matrix becomes challenging due to the creation of a high energy barrier to mixing. One method to counter this is by adopting a Hansen parameter approach whereby mutually compatible solvents are identified to facilitate blending of PDMS with a nanosheet dispersion.^[6] Once the solvent

1. Introduction

Polydimethylsiloxane (PDMS) is an interesting material for the development of novel functional composite materials owing to a range of useful properties. It is biocompatible, elastic,

is removed, the high viscosity of PDMS kinetically prevents reaggregation, and an isotropic composite can be formed.^[7] Naturally, the properties of a composite are determined primarily by those of the constituent materials. However, their relative volume fractions and their arrangement within the composite also play a significant role,^[8] with templated structures having been previously demonstrated to exhibit modifications to conductive properties in particular.^[9]

M. A. O'Mara, Dr. S. P. Ogilvie, Dr. M. J. Large, A. Amorim Graf, A. C. Sehnal, Dr. P. J. Lynch, Dr. A. A. K. King, Prof. A. B. Dalton
Department of Physics
University of Sussex
Falmer, Brighton BN1 9RH, UK
E-mail: M.OMara@sussex.ac.uk; A.B.Dalton@sussex.ac.uk

Dr. J. P. Salvage
Image Analysis Unit
University of Brighton
Brighton BN2 4GJ, UK
Dr. I. Jurewicz
Department of Physics
University of Surrey
Guildford GU2 7XH, UK

 The ORCID identification number(s) for the author(s) of this article can be found under <https://doi.org/10.1002/adfm.202002433>.

© 2020 The Authors. Published by WILEY-VCH Verlag GmbH & Co. KGaA, Weinheim. This is an open access article under the terms of the Creative Commons Attribution License, which permits use, distribution and reproduction in any medium, provided the original work is properly cited.

In this paper, we develop a process for preparing hierarchically structured nanocomposites of graphene and PDMS, which has the potential to be extended to a wide range of 2D layered materials and polymer matrices. Our method is based on Pickering emulsification, whereby two immiscible liquids are stabilized by solid particulates energetically trapped at their mutual interface.^[10–14] Pickering stabilization of liquid–liquid emulsions has been demonstrated with clays,^[15,16] graphene oxide,^[17] and graphitic multilayers.^[18–20] If either of the two liquid phases contains a polymer or polymer precursors then a solid structure can be produced, with the remaining solvents removed from the structure.^[20]

We identify a solvent system that enables the production of high-quality oil-in-water emulsions, in which graphene nanosheets assemble to stabilize PDMS-containing droplets. By modifying the processing conditions, we demonstrate that such emulsions can be cured into various morphologies, including microspheres and nanocomposite films. We

DOI: 10.1002/adfm.202002433

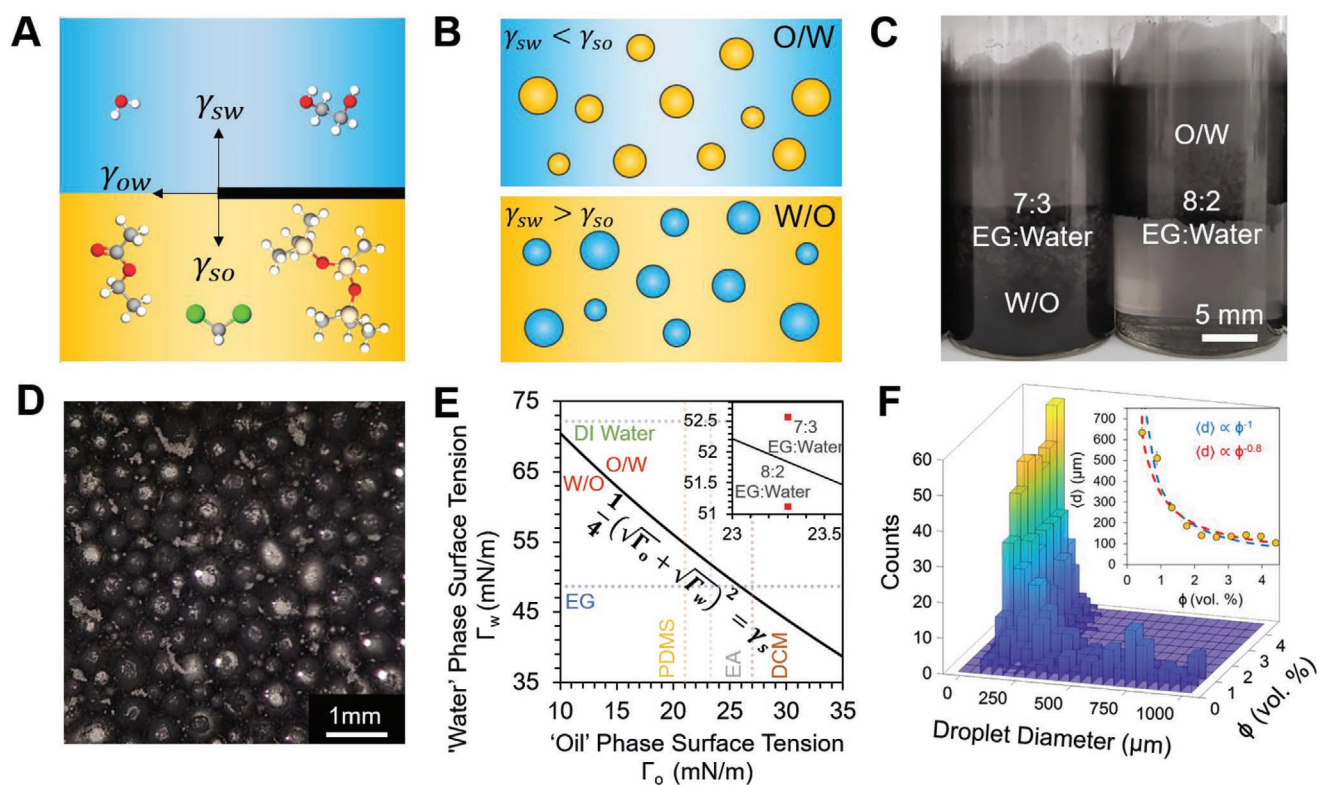


Figure 1. Emulsion formation and characteristics. A) Schematic diagram of an interfacial nanosheet within the present system. The interfacial energies are labeled at the three-phase boundary. B) Schematic of oil in water (o/w) and water in oil (w/o) emulsions, where the droplet phase is stabilized by a layer of nanosheets and the relative magnitudes of γ_{sw} and γ_{so} determine the orientation. C) Photograph of o/w and w/o emulsions where phase transition was brought about by altering the ratio of EG to water, and therefore γ_w . Scale bar 5 mm. D) Optical micrograph of a w/o emulsion with 0.44 vol% graphene relative to the droplet phase. Scale bar 1 mm. E) Phase diagram highlighting the parameter space for the system, where the phase inversion threshold marked (Equation (1)) is defined using the surface energy of graphene, $\gamma_s = 66 \text{ mJ m}^{-2}$. The surface tensions of water, EG, DCM, EA, and PDMS are marked. F) Relationship between graphene content ϕ and droplet size distribution. Inset: Average droplet diameter $\langle d \rangle$ versus ϕ .

investigate the underlying mechanisms of composite formation in our emulsified systems and show how they relate to the final electromechanical properties. We use this understanding to create highly elastic composites with a templated graphene network and characterize the electromechanical properties as a function of graphene content, before assessing their use as strain sensors.

2. Results

2.1. Emulsion Formation and Stability

The two-phase emulsion system utilized to prepare graphene-PDMS nanocomposites is illustrated in **Figure 1A**. A high surface energy “water” phase consists of water and ethylene glycol (EG), and a low surface energy “oil” phase contains dichloromethane (DCM), ethyl acetate (EA), and a commercial platinum-cure PDMS elastomer system. The oil phase solvents were identified by adopting a Hansen parameter matching approach; solvents intermediate to graphene and PDMS in Hansen space were identified as possible candidates. Of these, DCM and EA were selected as they both solvated PDMS and were found to sufficiently disperse a commercially available graphene powder. In principle, a similar methodology could

be applied to other polymers or resins to produce nanocomposites with layered nanomaterials. The water phase consists of deionized (DI) water and EG as this mixture is found to be immiscible with all blends of DCM:EA. Additionally, changing the ratio of DI water:EG tunes the surface energy of the water phase.

The relative surface energies of the oil and water phases (γ_o and γ_w , respectively) and the solid stabilizer (γ_s) dictate the stability of the emulsion. If the condition $\gamma_o < \gamma_s < \gamma_w$ is met, an emulsion may be formed. Since both EG and water have higher surface energies than graphene, and DCM, EA, and PDMS all have lower surface energies, all compositions of the system described in **Figure 1A** form stable emulsions. Further, the balance of interfacial tensions between the two liquid phases and the stabilizer dictate the orientation of the emulsion,^[10,21] where a water-in-oil (w/o) emulsion is formed if $\gamma_{so} < \gamma_{sw}$ and an oil-in-water (o/w) emulsion is formed if $\gamma_{so} > \gamma_{sw}$; this is shown schematically in **Figure 1B**. Modification of the solid-water interfacial energy γ_{sw} is achieved within the current system by modifying the ratio of DI water:EG, with EA comprising the oil phase; realizations of two system compositions that yield opposite phase orientations are shown in **Figure 1C**. Phase orientation is easily verified by droplet creaming or sedimentation, with reference to the relative densities of the phases. A demonstration of the droplets as formed is given in **Figure 1D**.

Figure 1E plots a phase diagram over the composition of the system in terms of the surface tensions of the water and oil phases, as these are directly measurable. The w/o-to-o/w inversion occurs when the energies of the solid–water and solid–oil interfaces are equal.^[21] It is more convenient to express the interfacial energies in terms of the more readily measurable surface energies of the solid, oil and water phases using a simple approximation such as $\gamma_{ab} = \gamma_a + \gamma_b + 2\sqrt{\gamma_a\gamma_b}$.^[17] We have shown that the emulsion inversion threshold can then be defined in terms of the three surface energies in the system (full derivation in Supporting Information), such that

$$\sqrt{\gamma_o} + \sqrt{\gamma_w} = 2\sqrt{\gamma_s} \quad (1)$$

A consequence of Equation (1) is that the determination of the surface energies of both liquid phases for system compositions either side of the inversion threshold allows for the calculation of the surface energy of the stabilizer. As shown in Figure 1C, we find the phase inversion threshold occurs between 70 and 80 vol% EG in the water phase. Utilizing the Wilhelmy plate method the surface tensions of EA ($\gamma_o = 23.3 \text{ mN m}^{-1}$) and DI water:EG mixtures ($\gamma_w = 52.6 \text{ mN m}^{-1}$ for the 70 vol% mixture and 51.1 mN m^{-1} for the 80 vol% mixture) were measured. We note that the surface energies of the liquids can be related to the directly measurable surface tensions by the surface entropy; $\Gamma = \gamma - TS$, where for liquids at 300 K $TS \approx 29 \text{ mN m}^{-1}$.^[22] Two limit values of the graphene surface energy are calculated using Equation (1), suggesting that the true value lies in the range $65.5 \text{ mN m}^{-1} < \gamma_{\text{graphene}} < 66.1 \text{ mN m}^{-1}$. This is consistent with relatively large, defect free graphene sheets,^[5] with potentially some influence of residual surfactant. We note that this value is somewhat lower than that expected for liquid-exfoliated graphene prepared in solvents such as *N*-methyl-2-pyrrolidone (NMP) where the surface energy matching is often taken to imply that $\gamma_{\text{graphene}} = 71 \text{ mN m}^{-1}$.^[5] Equation (1) is plotted as a solid black curve on Figure 1E with the defining value of $\gamma_{\text{graphene}} = 66 \text{ mN m}^{-1}$ taken from the above estimate.

Figure 1F shows a 3D histogram illustrating how the graphene volume fraction ϕ affects the droplet size distribution and average droplet diameter $\langle d \rangle$ of the emulsions. Since the total surface area available to stabilize the droplets increases with ϕ , we anticipate a decrease in $\langle d \rangle$ as the graphene loading increases; this scaling is clearly visible in the inset panel. Assuming uniform droplets, one can derive a relationship between ϕ and the droplet diameter d , namely^[23]

$$\phi = 6S/d \quad (2)$$

where S is the thickness of the graphene shell. Full details of the derivation are given in the Supporting Information. If we identify the droplet diameter d in Equation (2) with $\langle d \rangle$ plotted in Figure 1F, we see that the functional form $\langle d \rangle \propto \phi^{-1}$ is compatible with the data. This would suggest that S is constant and no overcoating of the interfaces occurs with additional graphene. However, we may also fit the data with a general power law of the form $\langle d \rangle \propto \phi^{-0.8}$; this suggests that the shell thickness is not constant but varies with loading level as $S \propto \phi^{0.2}$. This result is interpreted to mean that the degree of overcoating increases with graphene loading level.

Measuring $\langle d \rangle$ for a known inclusion of graphene gives us an estimate of the average shell thickness since from Equation (2) $\langle S \rangle = \phi \langle d \rangle / 6$ (provided d and S are treated as independent variables). For the data plotted in Figure 1F, we find that $\langle S \rangle = 0.7 \pm 0.2 \mu\text{m}$. We derive an alternative analytical expression for the shell thickness (see the Supporting Information), which yields a compatible value of $\langle S \rangle = 1.0 \pm 0.3 \mu\text{m}$.

2.2. Interdiffusion and Composite Formation

Based on the results of the compositional survey undertaken, a 1:1:2 volume mixture of PDMS:EA:DCM was found to maximize PDMS content, sufficiently reduce viscosity to enable effective homogenization, and yield reasonable density matching to minimize instability caused by sedimentation or creaming of droplets. Once emulsified, the PDMS-cure system contained within the oil phase can be readily crosslinked through application of heat. This results in graphene-coated PDMS balls or “G-balls” as depicted in Figure 2A, once the volatile solvents are removed and the solidified particles are washed. The G-balls may have a variety of uses, e.g., as a filler material for polymers where templating cannot be so readily achieved, or as precursors to other structures.

We observe a strong dependence of the morphological properties of the composite on the time the uncured emulsions were allowed to stand at room temperature. This is attributed to the fact that, given sufficient time, polymer chains are likely able to diffuse through the graphene shell and into neighboring droplets, eventually leading to a macroscopically continuous film. This transition is evident in the electron micrographs in Figure 2B. We note that analogous behavior is observed in other composite systems, such as the diffusion of graphene sheets into solvated rubber bands^[24] or the diffusion of carbon nanotubes into latex spheres.^[9]

The time taken for PDMS chains to diffuse into the graphene shell depends on the average thickness $\langle S \rangle$, but more so on the tortuosity of the shell structure. A simple model for the effective diffusivity D of the PDMS chains is derived (see the Supporting Information), taking into account the individual sheet thickness h , aspect ratio ρ_{aspect} , intersheet spacing b and interdiffusion time $\langle t_d \rangle$

$$D = \frac{\langle S \rangle^2}{\langle t_d \rangle} \left[\frac{h \left(1 + \frac{1}{2} \rho_{\text{aspect}} \right) + b}{h + b} \right]^2 = 3 \times 10^{-16} \text{ m}^2 \text{ s}^{-1} \quad (3)$$

We find good agreement between the predicted and measured values of $\langle S \rangle$ obtained from the SEM of fractured cross-sections in Figure 2B with $\langle S \rangle \approx 1.2 \mu\text{m}$. The aspect ratio of the flakes is estimated from the average length of each sheet divided by the average number of layers and the average interlayer spacing for graphite, i.e., $\rho_{\text{aspect}} = \langle L \rangle \langle N \rangle^{-1} c_{2D}^{-1} = 200$. The intersheet spacing b is taken to be $\approx 1 \text{ nm}$. Notably, D is almost 500 times lower than the self-diffusivity of $50\,000 \text{ g mol}^{-1}$ PDMS of $\approx 1.5 \times 10^{-14} \text{ m}^2 \text{ s}^{-1}$ (when adjusted to room temperature via the Arrhenius equation).^[25] This is consistent with similar results in the literature, in which DCM is shown to take ≈ 10 times longer to diffuse through a 10 wt% clay–PDMS

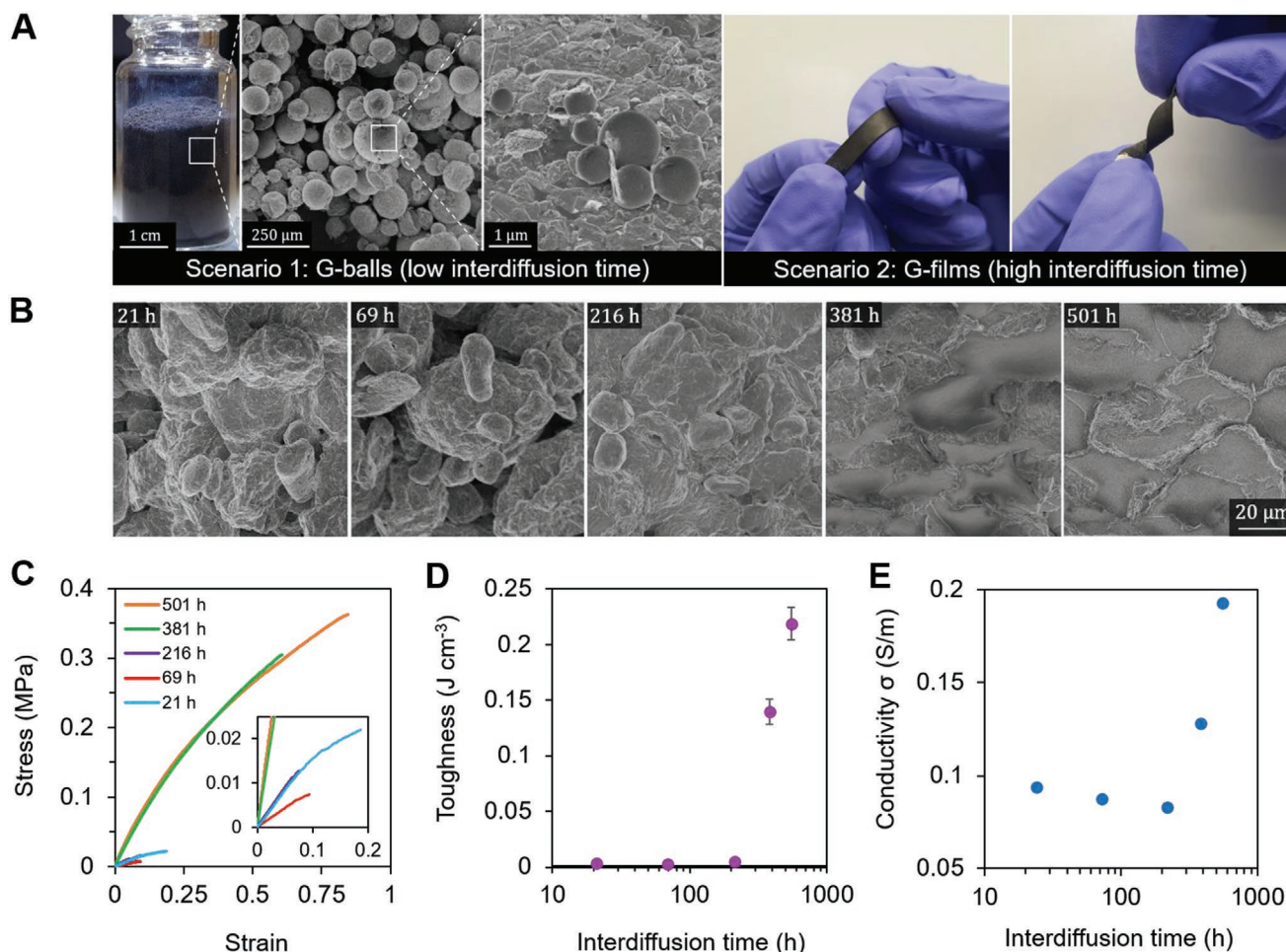


Figure 2. Morphological and electromechanical properties as a function of interdiffusion time for emulsion-based composites ($\phi = 7.4$ vol%). A) Photographs and SEM micrographs showing a distinct macroscopic transition from discrete balls to elastomeric composites as the interdiffusion time increases while the emulsions are in an uncured state. B) SEM micrographs versus interdiffusion time showing a transition from discrete balls (21–216 h) to an elastic composite (381–501 h) with a segregated network of graphene nanosheets. C) Representative stress–strain curves versus interdiffusion time. D) Toughness versus interdiffusion time. E) Conductivity versus interdiffusion time.

composite relative to pristine PDMS.^[26] We note that while the ratio of PDMS to curing agent (10:1) greatly effects the degree of crosslinking, we expect that the emulsion formation and diffusivity of the polymer is dominated by the viscosity of the oil phase at room temperature. One strategy to reduce the interdiffusion time is to use a lower molecular weight PDMS with a reduced viscosity and higher diffusion coefficient. Attempting to accelerate the diffusion process by increasing the temperature to 65 °C during the rest phase leads to the premature crosslinking of the silicone spheres, producing G-balls within 30 min, as shown in Figure 2A.

This calculation assumes that the interdiffusion time is the time taken for mechanical integrity to be conferred to the composites, $\langle t_d \rangle \approx 250$ h, beyond which an ≈ 100 time improvement in toughness can be clearly seen in Figure 2C,D. At low diffusion times, the performance is constant within statistical noise, while the mechanical toughness only increases drastically once a significant proportion of chains have diffused beyond the graphene shell, enabling interdroplet crosslinking and changing the dominant failure mechanism from overcoming

van der Waals adhesion to chain pull-out or scission.^[25] Further, we observe a doubling in conductivity upon the densification of the G-balls into a continuous film as shown in Figure 2E. This is attributed to the elimination of the void space between the G-balls increasing the electrical contact area between nanosheets and reducing the porosity of the composite film. Clearly, $\langle S \rangle$ and $\langle d \rangle$ play a vital role in composite formation and the resulting electromechanical properties.

2.3. Electromechanical Properties

The morphology of the conductive network in emulsion derived composites, visible in SEM of fractured cross-sections in Figure 2B, is considerably different from the graphene networks found in traditional randomly distributed composites. By virtue of the production method, the graphene is strongly confined at droplet interfaces in the liquid system, meaning that the network structure is preserved after curing. As such, with the graphene sheets all being confined to close proximity, it is

intuitive that electrical junctions will be of higher quality due to the reduced tunneling distance between nearest neighbors. In random percolating networks, a significant portion of the conductive filler does not contribute to the conducting path near the percolation threshold, resulting in a negligible contribution to macroscopic conductivity and inefficient use of the material, by comparison to the present system. In contrast, emulsion templated composites are largely self-similar over the loading levels studied, with the droplet size nearly constant only the shell thickness changes significantly. For $\langle t_d \rangle \gg 250$ h, we would expect the electromechanical properties to be dictated by loading level itself rather than the varying degrees of interdiffusion through the different shell thicknesses.

We observe greatly enhanced conductivity at all measured loading levels with no apparent percolation threshold, compared to randomly distributed graphene–silicone composites^[7] which represent state-of-the-art soft strain sensor materials. In the templated system, $\sigma = 0.027\phi$ with $R^2 = 0.94$ while in the random system $\sigma = 1.9 \times 10^{-15} (\phi - \phi_c)^{11.9}$ with $\phi_c = 1.75$, where ϕ here is in vol%. The lack of a well-defined percolation threshold is to be expected for systems where droplet size increases at lower loadings, resulting in macroscopic conductive pathways at all loadings capable of forming stable emulsions. Assembling the graphene network into a reduced volume (i.e., at the oil–water interface) reduces the total filler required

to achieve macroscopic conductive pathways, while interfacial tension aligns the graphene sheets to the tangent of the droplet surface. Both act to increase the number of conductive junctions and improve the quality of those junctions through superior intersheet contact when compared to randomly distributed networks.

To better understand the relationship between conductivity and loading level, we derive a resistor network model that treats each droplet surface and kernel as resistors in parallel, connected in series to a resistor representing the junction between neighboring droplets (see the Supporting Information). In the limit of low interdroplet resistance, such as these composites where the continuous phase is removed upon curing, it can be shown that the conductivity scales linearly with loading level. We find that $\sigma = 0.027\phi$ provides a robust fit to the data in **Figure 3A**, which suggests that the graphene conductive layer has an effective conductivity of 16 S m^{-1} based on the model calculation. Clearly this is significantly below what is typically expected of dense films of pristine graphene, further supporting the idea that the interfacial layers are interpenetrated with PDMS chains during film coalescence. Indeed, assuming that the random graphene–PDMS composites in **Figure 2A** are comparable in loading-dependent conductivity (as an estimate) the functional form of the data suggests the graphene volume fraction in the shell is around 23 vol%.

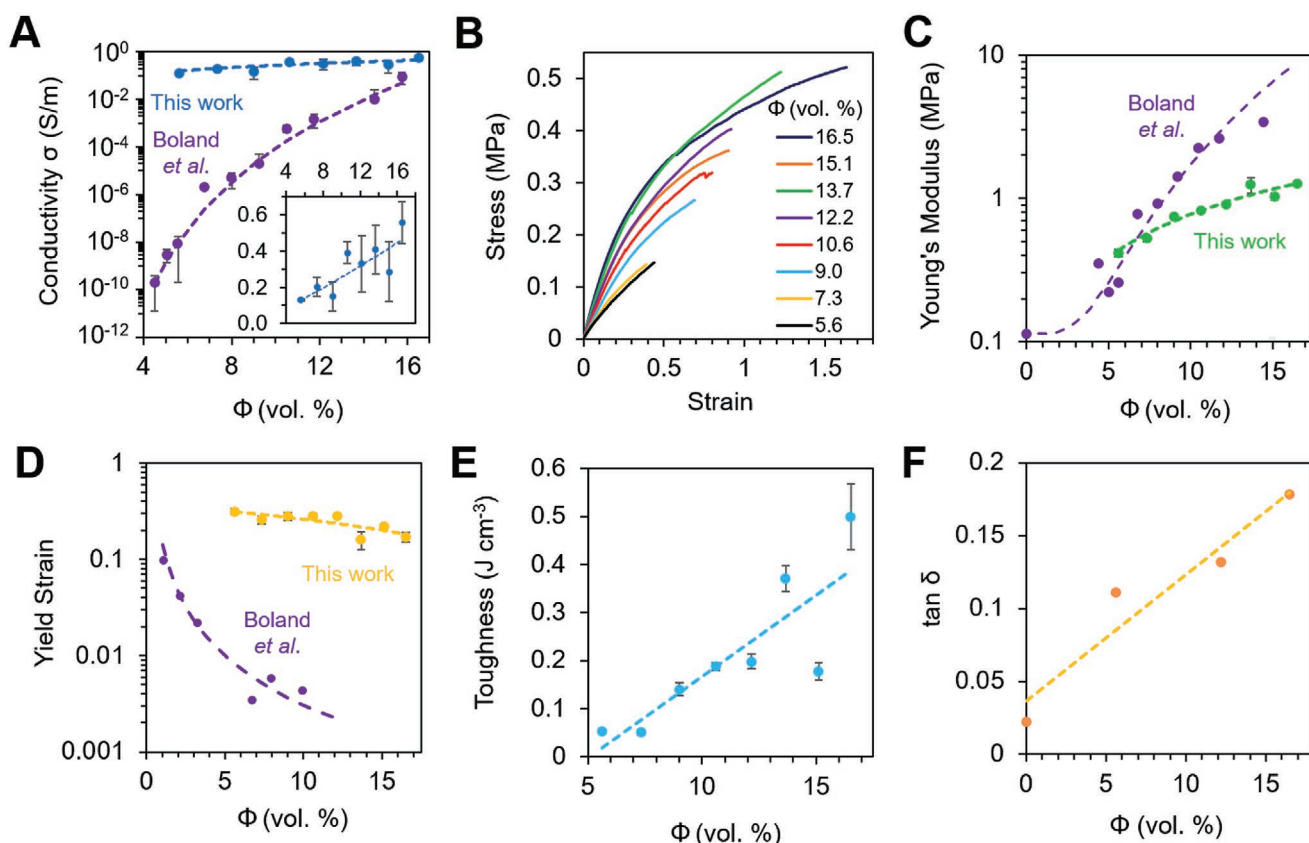


Figure 3. Electromechanical properties versus graphene loading level for emulsion based composite films. A) Conductivity versus loading level for templated emulsion composites and a random graphene–silicone composite system from the literature.^[7] B) Representative stress–strain curves shown as a function of loading level. C) Young's modulus versus loading level. D) Yield strain versus loading level. E) Toughness versus loading level. F) $\tan \delta$ versus loading level.

In terms of the mechanical properties of the composites, the stress–strain curves in Figure 2B exhibit a clear increase in the strain at break and Young’s modulus of the samples with increasing graphene loading. Figure 3C plots the Young’s modulus as a function of graphene loading, which shows a linear trend over the range of the data. The data for the random composites is plotted for comparison,^[7] wherein we observe a much greater increase of modulus with loading level. It is important to note, as was discussed by Boland^[27] that nanocomposites used for strain sensing need to remain sufficiently soft that they comply with the surface being measured; human skin. As such, the much weaker dependence of modulus on loading level observed in our system may prove beneficial to the design of on-skin sensors.

In contrast to the lower Young’s modulus observed in our templated samples than the isotropic samples, Figure 3D shows that our composites, which are based on a crosslinked elastomeric silicone, have a significantly higher yield strain. The yield strain is near constant, though both systems exhibit a decrease with increasing graphene content. We note that viscoelastic sensors with a significant viscous component will not recover once strained beyond the yield point.^[7] As our sensors are highly elastic, it is possible to operate the materials over a much wider strain range.

The structure of our composites, as highlighted in Figure 2B, consists of shells of graphene surrounding pristine PDMS “cores.” These shells, which are interdiffused with PDMS chains, are responsible for increasing the Young’s modulus (by virtue of interfacial stress transfer between the matrix and graphene) as well as the unusual increase in failure strain observed in Figure 3B. The increase in failure strain is likely a result of the reduction in overall crosslink density due to the penetration of the PDMS chains into the dense graphene shell, which interrupts interchain interactions both within and across the shell. Macroscopically, we observe a large increase in the toughness of the composites as a direct result; see Figure 3E. From this reasoning one also anticipates a modification to the loss tangent of the composite materials; by virtue of lowering the crosslink density, the samples behave in an increasingly viscous but less elastic fashion (rather than being highly elastic, as is the case with pristine PDMS). A comparison of several samples’ loss tangents obtained by dynamic mechanical analysis (DMA) with that of pristine PDMS films is shown in Figure 3F.

2.4. Strain Sensing and Calibration

The electrical properties and strain range of these composites demonstrated in Figure 2 naturally invite their application as strain sensors. Nanocomposites are attractive candidates for next-generation strain sensors due to their elasticity, but widespread adoption by industry has been hampered by nonlinear effects such as hysteresis and creep, making accurate, repeatable strain readouts an ongoing challenge.^[27]

Strain sensitivity is most usually characterized as the relative change in resistance per unit strain known as the gauge factor G ^[28]

$$G = 1 + 2\nu + \Delta\rho/\rho_0/\Delta\varepsilon = \Delta R/R_0\Delta\varepsilon = (1 + R/R_0)/\Delta\varepsilon \quad (4)$$

where ν is Poisson’s ratio, ρ is the resistivity, ρ_0 is the initial resistivity, R is the resistance, R_0 is the initial resistance, and ε is the applied strain. The gauge factor is a useful metric for characterizing sensitivity and reading out strain but applies only in the initial, linear region of R/R_0 , a rule not always followed in the literature.^[27,29] Commercial strain sensors are typically based on metal foil gauges in which a significant portion of their sensitivity arises from the changing geometry under strain, as described by the Poisson ratio, n . Since $n \approx 0.3\text{--}0.5$ for most materials, higher sensitivities are only accessible via piezoresistivity. Accuracy and reliability are preferred over sensitivity and strain range, with commercial gauge devices exhibiting a highly linear response. Their main weakness, however, is their relatively low sensitivity and strain range, with gauge factors ranging from 2 to 5 and maximum strains of 5% strain or less.^[30] As a result of this operating range, such sensors are applicable in use cases such as measuring the deflection of rigid mechanical structures.

For practical applications, it is only necessary to have a calibratable electrical response to applied strain, i.e., consistent, strictly monotonic and detectable. The range over which these conditions hold will be referred to as the working strain range. For exponential responses, using $R/R_0 = \Delta R/R_0 + 1$ allows for a single parameter function of the form $R/R_0 = e^{G_{\text{exp}}\varepsilon}$. This behavior is observed and depicted in Figure 4A, with R/R_0 as a function of strain for a high-loading composite ($\phi = 16.5$ vol%) shown over the working strain range. Plotting $R/R_0 = e^{G_{\text{exp}}\varepsilon}$ with $G_{\text{exp}} = 18.3$ provides an excellent fit ($R^2 = 0.998$), holding up to 80% strain. Since exponentials are linear to first order, G_{exp} satisfies the definition of the gauge factor in the low-strain linear regime.

Furthermore, G_{exp} appears to be independent of ϕ , fluctuating statistically randomly around 20 (Figure 4B). This suggests that the exponential response is attributed to the deformation of the conductive network and subsequent tunneling distance increase, with the average intersheet separation in our system remaining constant at all loading levels. The robustness of the exponential response suggests full calibration of the sensor is possible, facilitating accurate strain measurement even in the high-strain regime. We note that if the calibration phase gives $G_{\text{exp}} = 20$, an error of ± 1 in G_{exp} corresponds to an error of 5% in the calculated strain (see Figure S7 in the Supporting Information). Although the functional form is independent of loading level, the maximum R/R_0 and working strain range are determined by the conductivity and durability of the composite. Therefore, the highest loading level composites are the best candidates for strain sensing.

Although exponential responses have been reported in other nanocomposite strain sensors,^[28,29] G_{exp} is significantly lower in these systems, ranging from $G_{\text{exp}} = 1\text{--}5$ and valid up to varying degrees of strain. Interestingly, some workers observe an increase in G_{exp} at higher loadings albeit with significant scatter,^[24] while others find G_{exp} to be constant across all loadings.^[31] Despite the lack of standardization in reporting strain sensor performance,^[27] Figure 4C facilitates an easy comparison of our sensor with over 230 linear and nonlinear sensors found in the literature. The maximum sensitivity, $\Delta R/R_0\Delta\varepsilon$ is plotted against the working strain at which this is achieved. Linear sensors (blue dots) have a functional form that can be deduced, while nonlinear sensors (red dots) seldom

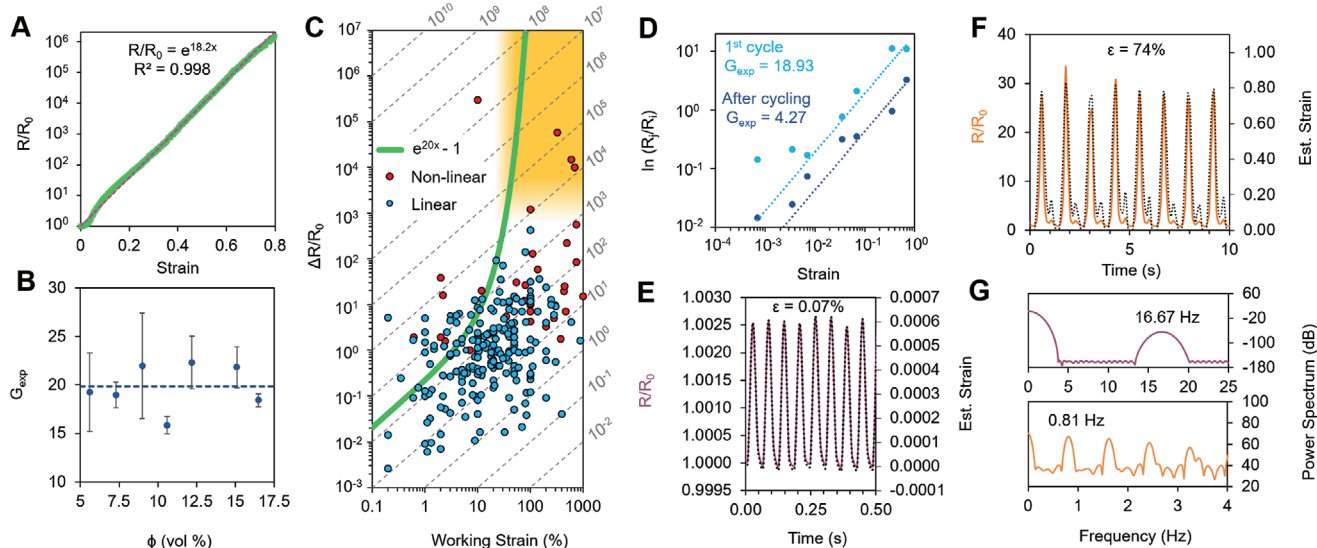


Figure 4. Strain sensing for emulsion-based composites. A) R/R_0 versus strain for $\phi = 16.5$ vol%. B) Sensitivity exponent $G_{\text{exp}} = \ln(R/R_0)/\epsilon$, shown to be independent of loading level. C) Strain sensitivity R/R_0 versus working strain, as reported in the literature. Blue dots indicate the maximum sensitivity and working strain range of linear sensors regimes while red dots indicate the maximum sensitivity and working strain range of nonlinear sensors extracted from over 230 references. The green line represents the response of our sensors, $R/R_0 = \exp(20\epsilon)$ while the gold region highlights the challenge region of high sensitivity and high working strain. D) Sensitivity decay of G_{exp} as a function of strain between the first cycle and >100 cycles later, converging to ≈ 4 . E) R/R_0 versus time for cyclic strain of 0.07% driven at 16.67 Hz. F) R/R_0 versus time for cyclic strain of 74% driven at 0.81 Hz. G) Fourier transform of (e) and (f), with clear peaks at the driving frequency.

have a functional form that can be defined. The green line, $\Delta R/R_0 = \exp(G_{\text{exp}}\epsilon) - 1$ with $G_{\text{exp}} = 20$ is representative of our best sensors and is plotted up to 80% strain. When compared to both linear and nonlinear strain sensors in the literature, our sensors exhibit the largest absolute change in resistance reported (Figure 4C). This is attributed to the efficient packing and distribution of the nanosheets, enabling excellent conductivity at lower loading levels and reducing the impact on the working strain range.

The cycling performance at low strain (0.07%, Figure 4D) and high strain (74%, Figure 4E) is assessed. The samples tested were able to withstand >1000 cycles at 36% strain and >100 cycles at 74% strain before failure. The driving frequency is easily extracted from the time series following a fast-Fourier transform (FFT) (Figure 4F) although a clear decrease in sensitivity is observed with increasing cycle number. Indeed, G_{exp} is found to decay to ≈ 4 after tens of cycles, after which it remains constant independently of strain magnitude as shown in Figure 4G. Interestingly, this value is in agreement with those reported elsewhere,^[24,31] which may indicate some universal phenomenon. As before, a constant value of $G_{\text{exp}} \approx 4$ after initial cycling enables an estimate of strain, as plotted on secondary axis in Figure 4D,E.

2.5. Bodily Motion Sensing

Strain scenarios specific to the human body, including finger bending, pulse and breathing are applied in Figure 5, with the electrical response examined. Figure 5A,B shows the sensor in a relaxed state when taped to the index finger, and in a strained state under maximum bending. In Figure 5C, we show

the electrical response to multiple fingers bends over a small ($<10^\circ$), medium ($\approx 45^\circ$) and large ($\approx 90^\circ$) bending radius. When fully extended (Figure 5A), the sensor is ≈ 4 cm, rising to ≈ 5 cm under large bending, or $\approx 25\%$ strain. The strain is approximated using $\epsilon = \ln(R/R_0)/G_{\text{exp}}$ and setting $G_{\text{exp}} = 20$, as determined in Figure 4 and is in good agreement with the expected strain as shown in Figure 4D,E.

In Figure 5D–I, the sensor is placed on both the neck and chest while the electrical response is recorded. When the sensor is gently pressed against the carotid artery (Figure 5D), the pulse is clearly detectable (Figure 5E) with a narrow peak at 59 bpm extracted from the Fourier transform (Figure 5F). When placed on the chest, the sensor is able to sense both high-strain, low-frequency modes associated with breathing and high-frequency, low-strain modes associated with a pulse. The fact that the pulse signal is easily discernible over the breathing mode speaks to the versatility of the device and its potential as a biomedical sensor. Inset to Figure 5E is the pulse waveform once the breathing induced baseline drift is removed. This is also subject to a Fourier transform, revealing a maximum at 65 bpm (Figure 5F), typical of a resting heart rate.

3. Conclusion

We have developed a method of incorporating large quantities of graphene nanosheets into a PDMS matrix in a structured, controllable fashion that results in excellent electromechanical properties ideally suited to strain sensing applications. We have mapped out the underlying principles of the technique to enable additional optimization, and in principle one may extend our approach to other polymers and nanomaterials of interest.

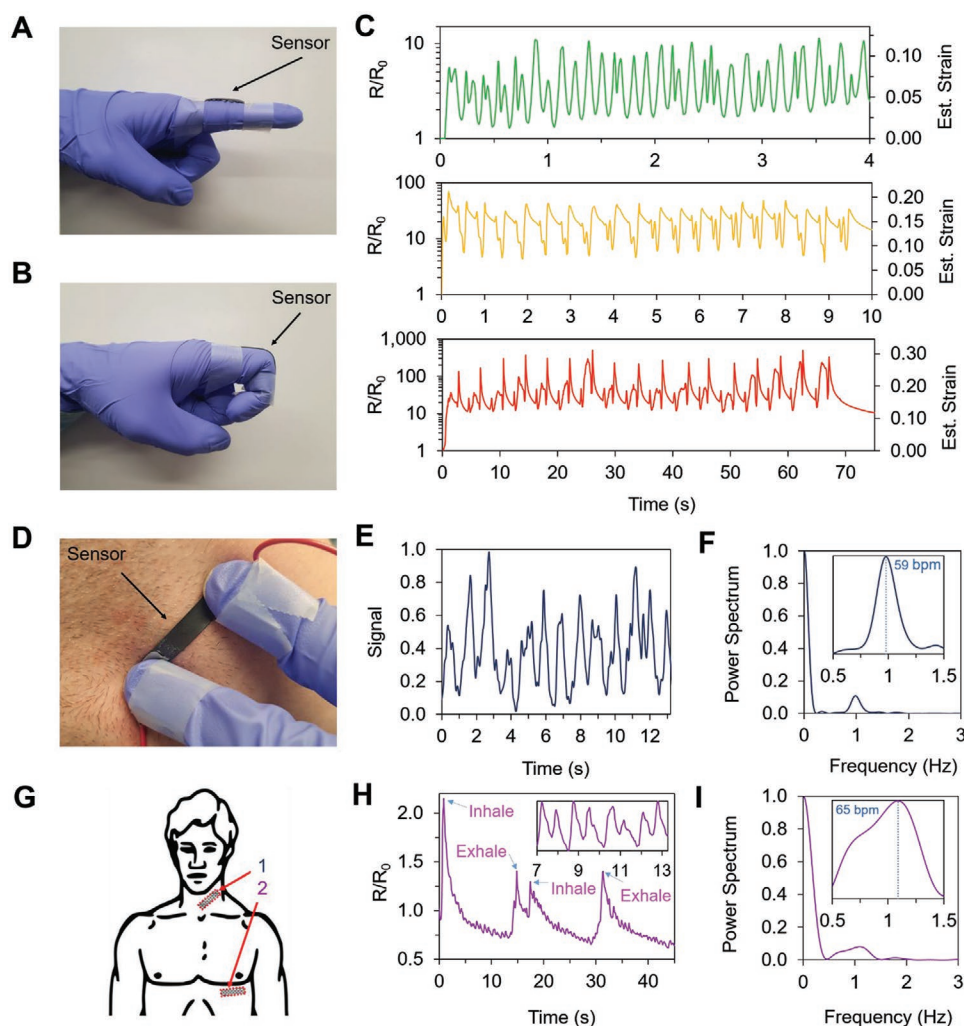


Figure 5. Biomechanical strain sensing for emulsion-based sensors. A) Sensor in relaxed position with finger fully extended, attached using scotch tape. B) Sensor under full extension for finger bending. C) Relative resistance change for “small,” “medium,” and “large” finger bending with the estimated strain on the second axis. D) Photo of sensor placement over the carotid artery (1). E) Electrical response taken from the carotid artery (1) with baseline drift subtracted. F) FFT of (E). G) Sensor placement for pulse (1) and breathing a pulse (2) measurements. H) Relative resistance change taken from the chest (2) under deep breathing. Inset: Pulse signal extracted and baseline drift subtracted. I) FFT of (H).

The morphology of the emulsion-templated network imbues the composite with conductivities several orders of magnitude higher than isotropic composites at low loading levels (≈ 5 vol%) and is likely responsible for the robust exponential sensitivity to strain. Able to detect strains $<0.1\%$ and $>80\%$, we demonstrate sensor measurements of pulse, joint motion, and ventilation using the composites described. This promising technology may prove especially useful in established fields such as health-care, sports performance monitoring and rapidly growing fields such as soft robotics.

4. Experimental Section

To establish the phase inversion point in Figure 1C and plot the phase inversion boundary in Figure 1E, 100 mg of graphene powder was added to 10 mL of ethyl acetate and bath sonicated. A mixture of EG:DI water was added in ratios ranging from 10:0 to 0:10 in 10 vol% increments such that the water phase also totals 10 mL. The mixture was then shaken

vigorously for 30 s and was characterized as o/w or w/o by the buoyancy of the droplet phase, as the water phase was denser than the oil phase.

To establish the droplet size dependence on graphene content, w/o emulsions was opted as seen in Figure 1D,F. This is because graphene has a surface energy between air and “water” and will seek to stabilize that interface. This water–air interface is only present for oil in water emulsions and will lead to a continuous film of graphene at the surface, obscuring the contents below. For w/o emulsions, however, hydrophobic containers must be used to prevent the droplets from bursting as the high surface tension water phase will seek to stabilize the even greater surface energy disparity between glass and graphene. To ensure a w/o emulsion, the water phase was consisted of 100% DI water, while the oil phase was consisted of 1:1:2 PDMS:EA:DCM. 5–50 mg (in 5 mg increments) of graphene powder was weighed out into hydrophobic (silanized) glass vials before 0.5 mL of DI water was added and sonicated together. 3.5 mL of the oil phase was added and the mixture was shaken vigorously. The newly formed emulsion was poured into a hydrophobic (PTFE) cubic well 4 cm³ in volume and images were taken under 10 \times magnification. Using ImageJ software, 100 droplets were measured along their longest dimension for each sample, the average was taken and the standard error was calculated.

A Hansen parameter approach was used to identify cosolvents for graphene (Thomas Swan, Premium Elicarb graphene powder) and PDMS (Farnell UK, Qsil b, 4500 mPa s) (see the Supporting Information). Dichloromethane (Sigma Aldrich, 1.325 g mL⁻¹, 0.413 mPa s at 25 °C) and ethyl acetate (Sigma Aldrich, 0.902 g mL⁻¹, 0.426 mPa s at 25 °C) were found to be capable of thinning the PDMS and dispersing pre-exfoliated graphene well enough to emulsify the oil–water mixture. It was found that 2:1:1 parts DCM:EA:PDMS by volume offered a reasonable compromise toward matching the density of the oil and water phases, lowering the viscosity of the oil phase and maintaining an acceptable solids content.

The graphene powder used was a commercially available product, with the following taken from the datasheet: average particle size distribution: $D_{10} = 1 \mu\text{m}$, $D_{50} = 4 \mu\text{m}$, and $D_{90} = 10 \mu\text{m}$. Sheet resistance = typically <25 $\Omega \square^{-1}$ normalized to 25 μm . Surface area = $\approx 50\text{--}100 \text{ m}^2 \text{ g}^{-1}$ (BET). $D/G < 0.15$ (very low defect material). % Residue < 1%. % Surfactant < 3%.

Graphene powder was added to DCM (Table S1 in the Supporting Information) and bath sonicated (Grant XUB Bath Sonicator) at 10 °C for 1 h before being added to the ethyl acetate-swelled PDMS and homogenized via vigorous shaking for 30 s. Ethylene glycol was then added such that the o:w ratio is 40:60 v/v before shear mixing (Silverson L5M-A) at 10 000 rpm for 2 min. The newly formed emulsions were resealed and allowed to interdiffuse for a time t_{diff} before being reshaken for 30 s and poured into a glass petri dish. The emulsions were then placed in an oven at 30 °C for 1 h before raising the temperature by 10 °C every hour until 70 °C was reached and subsequently maintained overnight, unless otherwise stated. This was to avoid turbulent boiling of DCM and EA from the PDMS when curing.

To determine the morphological time dependence of the composites in Figure 2, five identical o/w emulsions were made using this method, with $\phi = 7.3 \text{ vol}\%$. They were each allowed to stand for 21–501 h, before being poured into glass Petri dishes and cured through incremental increases in temperature. SEM (Zeiss SIGMA field-emission gun SEM) microscopy and Raman spectroscopy (Renishaw inVia) microscopy were performed on stress-fractured cross-sections. Electrical conductivity was measured using a Keithley 2126B probe station with silver electrodes painted on the ends of several strips cut $\approx 5\text{--}7 \text{ mm}$ wide and $\approx 25\text{--}30 \text{ mm}$ long from each sample to minimize contact resistance. The thickness of each sample was measured using a screw gauge, before strain-to-failure testing takes place on a mechanical testing stage (Texture Analyser, Stable Microsystems).

To determine the effect of graphene content on composite electromechanical properties, 12 o/w emulsions were prepared at various loading levels described in Table S1 in the Supporting Information. So as to ensure elastomeric composites, the samples were cast after $\approx 2500 \text{ h}$ (107 days). At the time of casting, emulsions containing 2 vol% of graphene or less had cured in situ, while $\phi = 3.8 \text{ vol}\%$ had partially cured. Conversely, for $\phi > 10.6 \text{ vol}\%$, the aforementioned curing profile was insufficient to harden the composites likely due to reduced crosslink density near to the graphene network. For this reason, all samples with $\phi = 5.6 \text{ vol}\%$ and above were held in the oven for an additional night at 70 °C.

The electrical properties of these composites were measured as they were strained until failure. The samples were insulated against the TA using sandpaper while establishing an electrical connection to the Keithley probe station via crocodile clips attached to tin foil strips pressed against the silver-painted composite electrodes during clamping. An exponential fit was applied to R/R_0 over an appropriate strain range ($R^2 > 0.95$). The average exponent was plotted in Figure 4B as a function of the graphene loading level.

Subsequent strain sensing measurements were performed on the highest loading level samples, i.e., $\phi = 16.5\%$ by volume, due to their superior conductivity and durability as discussed in the main text.

Supporting Information

Supporting Information is available from the Wiley Online Library or from the author.

Acknowledgements

The authors would like to thank Alliance Rubber Co. for funding and supporting this work. For all experiments involving a human participant, informed signed consent was obtained from the volunteer.

Conflict of Interest

The authors declare no conflict of interest.

Keywords

composites, emulsions, graphene, silicone, strain sensing

Received: March 16, 2020

Revised: April 27, 2020

Published online: June 4, 2020

- [1] A. Mata, A. J. Fleischman, S. Roy, *Biomed. Microdevices* **2005**, *7*, 281.
- [2] S. H. Tan, N.-T. Nguyen, Y. C. Chua, T. G. Kang, *Biomicrofluidics* **2010**, *4*, 032204.
- [3] H. Hillborg, J. F. Ankner, U. W. Gedde, G. D. Smith, H. K. Yasuda, K. Wikström, *Polymer* **2000**, *41*, 6851.
- [4] A. Ferguson, I. T. Caffrey, C. Backes, J. N. Coleman, S. D. Bergin, *Chem. Mater.* **2016**, *28*, 6355.
- [5] A. Ferguson, A. Harvey, I. J. Godwin, S. D. Bergin, J. N. Coleman, *2D Mater.* **2016**, *4*, 015040.
- [6] Y. Hernandez, M. Lotya, D. Rickard, S. D. Bergin, J. N. Coleman, *Langmuir* **2010**, *26*, 3208.
- [7] C. S. Boland, U. Khan, G. Ryan, S. Barwich, R. Charifou, A. Harvey, C. Backes, Z. Li, M. S. Ferreira, M. E. Mobius, R. J. Young, J. N. Coleman, *Science* **2016**, *354*, 1257.
- [8] A. J. Marsden, D. G. Papageorgiou, C. Vallés, A. Liscio, V. Palermo, M. A. Bissett, R. J. Young, I. A. Kinloch, *2D Mater.* **2018**, *5*, 032003.
- [9] I. Jurewicz, P. Worajittiphon, A. A. K. King, P. J. Sellin, J. L. Keddie, A. B. Dalton, *J. Phys. Chem. B* **2011**, *115*, 6395.
- [10] Y. Chevalier, M.-A. Bolzinger, *Colloids Surf. A* **2013**, *439*, 23.
- [11] R. McGorty, J. Fung, D. Kaz, V. N. Manoharan, *Mater. Today* **2010**, *13*, 34.
- [12] Q. Monégier du Sorbier, A. Aimable, C. Pagnoux, *J. Colloid Interface Sci.* **2015**, *448*, 306.
- [13] T. Ngai, S. Bon, *Particle-Stabilized Emulsions and Colloids: Formation and Applications*, RSC Soft Matter Series, Royal Society of Chemistry, Cambridge **2014**.
- [14] Y. Yang, Z. Fang, X. Chen, W. Zhang, Y. Xie, Y. Chen, Z. Liu, W. Yuan, *Fron. Pharmacol.* **2017**, *8*, 287.
- [15] N. P. Ashby, B. P. Binks, *Phys. Chem. Chem. Phys.* **2000**, *2*, 5640.
- [16] S. Cauvin, P. J. Colver, S. A. F. Bon, *Macromolecules* **2005**, *38*, 7887.
- [17] Y. He, F. Wu, X. Sun, R. Li, Y. Guo, C. Li, L. Zhang, F. Xing, W. Wang, J. Gao, *ACS Appl. Mater. Interfaces* **2013**, *5*, 4843.
- [18] M. J. Large, S. P. Ogilvie, M. Meloni, A. Amorim Graf, G. Fratta, J. Salvage, A. A. K. King, A. B. Dalton, *Nanoscale* **2018**, *10*, 1582.
- [19] S. J. Woltornist, J.-M. Y. Carrillo, T. O. Xu, A. V. Dobrynin, D. H. Adamson, *Macromolecules* **2015**, *48*, 687.
- [20] S. J. Woltornist, D. Varghese, D. Massucci, Z. Cao, A. V. Dobrynin, D. H. Adamson, *Adv. Mater.* **2017**, *29*, 1604947.

- [21] S. P. Ogilvie, M. J. Large, A. J. Cass, A. A. Graf, A. C. Sehnal, M. A. O'Mara, P. J. Lynch, J. P. Salvage, A. A. K. King, A. B. Dalton, <https://arxiv.org/abs/2005.06330>.
- [22] J. Keddie, A. F. Routh, *Fundamentals of Latex Film Formation Processes and Properties*, Springer, New York **2010**.
- [23] F. M. Fowkes, *J. Phys. Chem.* **1962**, *66*, 382.
- [24] C. S. Boland, U. Khan, C. Backes, A. O'Neill, J. McCauley, S. Duane, R. Shanker, Y. Liu, I. Jurewicz, A. B. Dalton, J. N. Coleman, *ACS Nano* **2014**, *8*, 8819.
- [25] J. Mazan, B. Leclerc, N. Galandrin, G. Couarraze, *Eur. Polym. J.* **1995**, *31*, 803.
- [26] Q. Liu, D. De Kee, *J. Non-Newtonian Fluid Mech.* **2005**, *131*, 32.
- [27] C. S. Boland, *ACS Nano* **2019**, *13*, 13627.
- [28] T. G. Beckwith, N. L. Buck, R. D. Marangoni, *Mechanical Measurements*, 3rd ed., Addison-Wesley, Reading, MA **1982**.
- [29] Z. Tang, S. Jia, F. Wang, C. Bian, Y. Chen, Y. Wang, B. Li, *ACS Appl. Mater. Interfaces* **2018**, *10*, 6624.
- [30] M. Amjadi, A. Pichitpajongkit, S. Lee, S. Ryu, I. Park, *ACS Nano* **2014**, *8*, 5154.
- [31] R. Zhang, M. Baxendale, T. Peijs, *Phys. Rev. B* **2007**, *76*, 195433.